Response of Methylammonium Lead Iodide to External Stimuli and Caloric Effects from Molecular Dynamics Simulations

Shi Liu*,† and R. E. Cohen*,†,‡

†Extreme Materials Initiative, Geophysical Laboratory, Carnegie Institution for Science, Washington, DC 20015-1305, United States
‡Department of Earth and Environmental Sciences, Ludwig Maximilians Universität, Munich 80333, Germany

Ⓢ Supporting Information

ABSTRACT: The power conversion efficiency for solar cells fabricated using organometal halide perovskites (OMHPs) has risen to more than 20% in a short span of time, making OMHPs promising solar materials for harnessing energy from sunlight. The hybrid perovskite architecture that consists of organic molecular cations and an inorganic lattice could also potentially serve as a robust platform for materials design to realize functionalities beyond photovoltaic applications. Taking methylammonium lead iodide ($MAPbI_3$) as an example, we explore the response of organometal halide perovskites to various stimuli, using all-atom molecular dynamics simulations with a first-principles-based interatomic potential. We find that a large electric field is necessary to introduce a sizable molecular ordering at room temperature in unstrained $MAPbI_3$. Molecular dipoles in epitaxially strained $MAPbI_3$ are more susceptible to an electric field. We also report various caloric effects in $MAPbI_3$. The adiabatic thermal change is estimated directly by introducing different driving fields in the simulations. We find that $MAPbI_3$ exhibits both electrocaloric and mechanocaloric effects at room temperature. Local structural analysis reveals that the rearrangement of molecular cations in response to electric and stress fields is responsible for the caloric effects. The enhancement of caloric response could be realized through strain engineering and chemical doping.
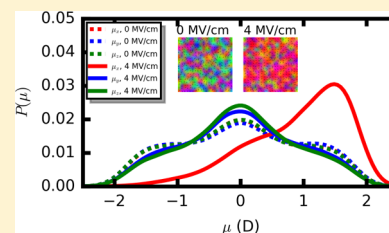
INTRODUCTION

Organometal halide perovskites (OMHPs) are promising candidates for low-cost-to-power photovoltaic technologies. They are now at the frontier of renewable energy research for their record speed of increasing power conversion efficiency.[1−4] The sharp rise in conversion efficiency from 3.8%[1] in 2009 to 22.1% in 2016 (KRICT, South Korea)[4] is unmatched by any other solar-cell technologies. Since OMHP crystals are easily grown,[5] they could serve as a robust platform for active materials beyond photovoltaic applications. Represented by methylammonium lead iodide ($MAPbI_3$), these materials have the ABX_3 perovskite structure with an organic monovalent cation at A-site, a divalent metal at B-site, and a halide anion at X-site. The molecular cation has a permanent dipole and interacts with the inorganic BX_3 scaffold mostly through van der Waals interactions and hydrogen bonding.[6,7] Further functionalities of OMHPs have been proposed, ranging from thermoelectrics[8,9] and spintronics[10,11] to light-emitting diodes and lasers.[12,13]

Compared to inorganic perovkites, one unique structural feature of OMHPs comes from the A-site organic molecules that may undergo significant rearrangement at room temperature due to their small rotational barrier.[14,15] The ordering and rotations of organic cations are suggested to be relevant to the superior photovoltaic performance of OMHPs.[11,16−18] Several microscopic mechanisms have been proposed. Local alignment of molecular dipoles could give rise to spontaneous polarization and polar domains at the nanoscale; the internal electric field at domain boundaries of the polarization gradient may facilitate electron−hole separation and suppress recombination,[16,17]

which are potentially responsible for the slow charge recombination and long charge diffusion lengths.[19−21] Driven by the strong spin−orbit coupling of Pb atoms, the Rashba effect in locally polarized domains could result in spin-allowed and spin-forbidden recombination channels, with the spin-forbidden path exhibiting a slow recombination rate because of the mismatch of spin and momentum.[11] The fluctuating electrostatic potential resulting from the randomly oriented molecular dipoles causes the spatial separation of charge densities of the conduction band minimum and the valence band maximum, thus reducing the carrier recombination rate.[18] The dynamics of molecular cations that directly influence the length/time scale of polar domains therefore will affect the significance of those polar-domain-based microscopic models for carrier dynamics.[22,23] Ionic conduction is another mechanism that can influence the photovoltaic performance. The diffusion of charged defects leads to space charge regions close to the contacts.[24,25] First-principles calculations show that iodine vacancy (V_I^+) is the dominate diffuser in $MAPbI_3$, with low diffusion barrier[26] and high hopping rate at 300 K.[27] The ionic diffusion could serve as another source of polarization, likely to be responsible for the current−voltage hysteresis in $MAPbI_3$ solar cells.[28−30]

The rotational dynamics of MA^+ cations in $MAPbI_3$ are intimately related to a question that is under active debate: whether $MAPbI_3$ possess long-range/time-scale ferroelectric ordering due to orientational aligment of MA^+ cations at room

temperature. Though the presence of switchable polar domains in MAPbI$_3$ is indicated by several piezoresponse force microscopy/atomic force microscopy experiments,[31−33] a number of works also suggest the absence of ferroelectricity at room temperature[24,34] or poor polarization retention after switching.[35] Neutron powder diffraction studies reveal that MA$^+$ cations at room temperature are rotationally disordered, and could direct toward the face of the distorted cubic PbI$_3$ framework,[36] which is consistent with elastic and quasi-elastic neutron scattering results: MA$^+$ cations exhibit 4-fold rotational symmetry of the C−N axis in tetragonal phase.[23] Both ab initio[30,37,38] and classical molecular dynamics simulations[39] reveal the fast reorientational dynamics of molecular cations at room temperature with relaxation times in the range of 1−5 ps, consistent with experimental works with NMR,[40] millimeter-wave spectroscopy,[41] and neutron diffraction.[23,42] Recent DFT calculations demonstrate a large number of structural local minima with differently oriented polarization directions for orthorhombic MAPbI$_3$.[43] This supports a disordered super-paraelectric-like behavior, being spontaneously polarized at the nanoscale but polar-compensated (zero-polarization) at the macroscale. As a ferroelectric is characterized by an electric-field-switchable spontaneous polarization, one goal of this work is to understand the molecular ordering in response to an external electric field.

There has been a surge of interest in using caloric materials to develop environmentally friendly solid-state cooling technology as an alternative to traditional vapor-compression technology that relies on refrigerants with high global-warming potential (hydrofluorocarbons and hydrochlorofluorocarbons).[44−48] Caloric effects refer to the phenomena in which the temperature of the materials changes in response to the change of an external driving field.[46] There are different types of caloric effects, depending on the nature of the driving field. The electrocaloric effect (ECE) is driven by an applied electric field, whereas the mechanocaloric effect is induced by an applied mechanical stress (the elastocaloric effect is driven by a uniaxial stress, and the barocaloric effect is driven by an isotropic stress). Magneto-caloric materials will have reversible thermal changes in response to changes in the applied magnetic field.[46] A cooling cycle is realized through two constant-entropy (adiabatic) transitions and two constant-driving-force transitions (Figure 1).[44] It is
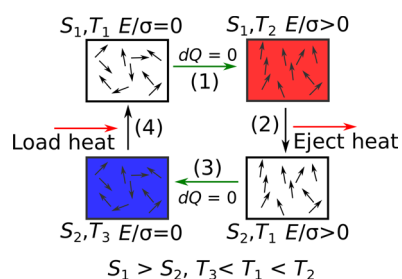
Figure 1. Schematic of a caloric cooling cycle involving two adiabatic processes (steps 1 and 3) and two constant-driving-field (E, electric field; σ, stress field) processes (steps 2 and 4).

known that the ECE could occur in any insulator with a large, temperature-dependent, dielectric susceptibility.[48] Relaxor ferro-electrics characterized by disordered fluctuating polarization entities and polar nanoregions are suggested to have high ECE.[49] Experiments have demonstrated that organic poly(vinylidene fluoride-trifluoroethylene) relaxor copolymer and inorganic La-

doped Pb(Zr,Ti)O$_3$ have giant ECEs in comparison to their normal ferroelectric counterparts.[50] The intrinsic dipoles afforded by the molecular cations may give rise to ECE in OMHPs. Motivated by the similarity of OMHPs with relaxor ferroelectrics that have many applications ranging from trans-ducers to caloric applications,[51] we explore the intrinsic response of MAPbI$_3$ to various external stimuli and the associated caloric effects with all-atom molecular dynamics (MD) simulations. We study both electrocaloric and mechanocaloric effects under different temperatures. The temperature change is estimated directly by adiabatically applying driving fields in MD simulations.

■ COMPUTATIONAL METHODS

We used a classical model potential (MYP) derived from first principles, recently developed by Mattoni et al.[39] The interatomic potential of MAPbI$_3$ consists of organic−organic, organic−inorganic, and inorganic−inorganic interactions. The organic−organic interaction includes both the intramolecular and intermolecular interactions described by the standard AMBER force field. The interactions within the inorganic Pb−I scaffold are described by a Buckingham potential. The interactions between the MA$^+$ cation and the PbI$_3$ sublattice are described as the sum of Buckingham, electrostatic, and Lennard-Jones potentials (see details in ref 39). The force field parameters are fitted to a data set obtained by density functional theory calculations with the PBE exchange−correlation func-tional. The MYP potential is able to reproduce the DFT cohesive energy curve under hydrostatic deformations (bulk modulus = 18 GPa) and the rotational barrier for molecules in the cubic phase at 0 K, and it also captures experimental orthorhombic−tetragonal and tetragonal−cubic phase transitions. The relaxa-tion times of reorientational dynamics of MA$^+$ cations estimated using the MD trajectories obtained with this potential also agree with experiments[23,40−42] and recent ab initio MD calcula-tions.[37,38] Though the model potential is not directly optimized with regard to the vibrational properties, a recent study showed that it could qualitatively reproduce DFT vibrational spectrum.[52] The MYP classical potential is also successfully applied to study ionic transport in crystalline MAPbI$_3$.[79] The success of this first-principle-derived ionic model potential is partly due to the strong ionic bonding character in MAPbI$_3$[53] and the weak electronic coupling between the organic molecules and the inorganic PbI$_3$ scaffold.[14,54,55]

We carried out MD simulations on a 20 × 20 × 20 pseudocubic supercell (96 000 atoms and one formula unit for each pseudocubic unit cell). The temperature is controlled by a Nosé−Hoover thermostat, and the pressure is maintained at 0.0 MPa by the Parrinello−Rahman barostat implemented in LAMMPS.[56] A 0.5 fs time step is used and the system is equilibrated for more than 2 ns before turning on the external driving field. During the application of the driving field, a large inertial parameter, M_s, is used for the thermostat (Tdamp = 5 ns in LAMMPS) to prevent heat transfer between the system and the thermostat, simulating an adiabatic process. The original model potential is developed on the basis of DLPOLY code[57] with standard Ewald summation for computing Coulombic interactions. We benchmarked the thermal evolution of pseudocubic lattice constant with LAMMPS using a particle−particle particle−mesh solver[58] for the long-range interactions (with desired relative error of 0.22 × 10^{-6} eV/Å in forces) and obtained the same results (see the Supporting Information) reported in ref 39. We do not consider the orthorhombic phase
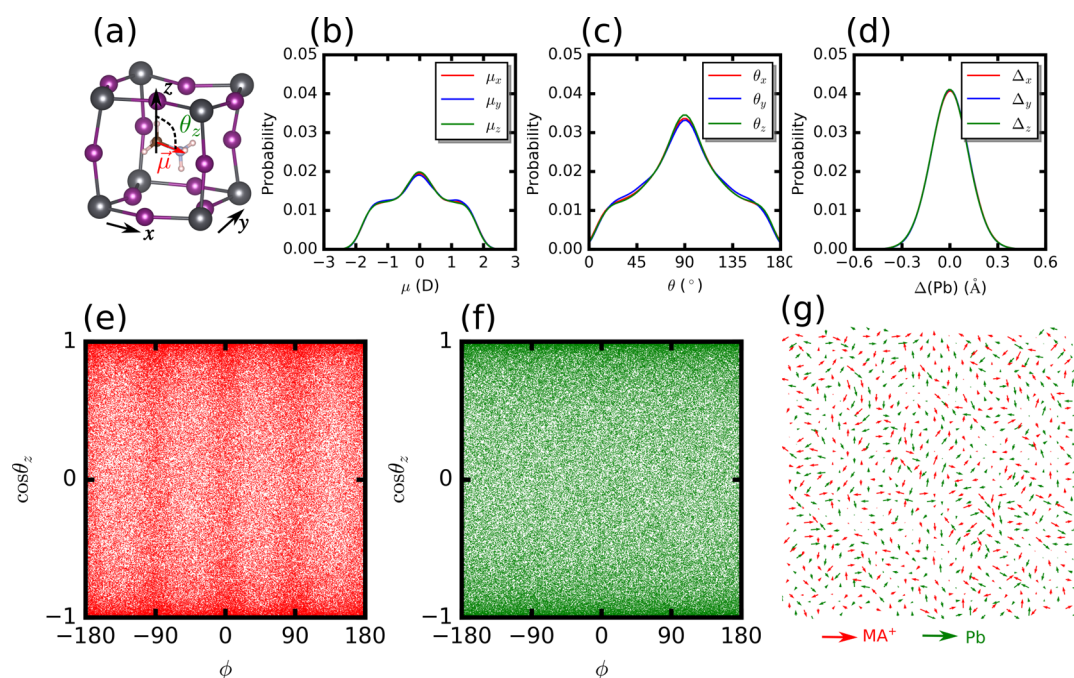
Figure 2. Structure of MAPbI$_3$ at zero field and 300 K. (a) Schematic of a pseudocubic unit cell of MAPbI$_3$. Probability distribution functions for (b) component-resolved molecular dipoles, (c) angles between molecular dipoles and Cartesian axes, and (d) Pb displacements from the center of their I6 cages. Directional maps (ϕ, cos θ) for (e) molecular dipoles and (f) dipoles due to Pb displacements. The maps are obtained by recording the orientations of all the 8000 MA$^+$ cations and 8000 Pb atoms, sampled every 0.5 ps from a 10 ps trajectory at 300 K obtained in constant-temperature constant-pressure simulations. (g) The snapshot of molecular dipoles (red arrows) and Pb-displacement dipoles (green arrows) in the *xy* plane.
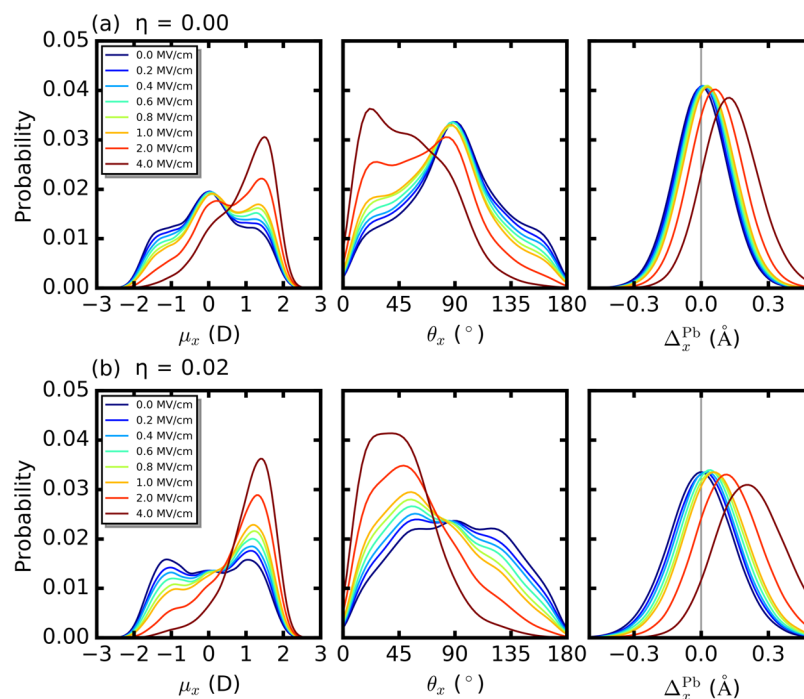
Figure 3. Structural changes of MAPbI$_3$ in response to electric field under (a) zero stress and (b) 2% compressive epitaxial stress in the *yz* plane. The electric field is applied along the +*x* direction. The changes in structure are captured by the changes in probability distribution functions of *x*-component molecular dipoles (μ_x), the angle between the molecular dipole and +*x* axis (θ_x), and Pb displacement along *x* (Δ_x^{Pb}).

that occurs below 160 K,[59] as we are focused on possible room-temperature applications.

■ RESULTS AND DISCUSSIONS

Structure of MAPbI$_3$ at Zero Field. We first examine the structural features of MAPbI$_3$ at 300 K in the absence of an

electric field (Figure 2), by calculating the probability distribution functions (P) of molecular dipoles along the Cartesian axes (μ_x, μ_y, and μ_z), angles between the molecular dipole and Cartesian axes (θ_x, θ_y and θ_z), and displacements of Pb atoms with respect to the center of I6 cages (Δ_x, Δ_y, and Δ_z). We find that both $P(\mu_i)$ and $P(\theta_i)$ ($i = x, y, z$) exhibit

broad and symmetric distributions, leading to a zero macroscopic polarization. The instantanous molecular orientation $\hat{n}$ can be described by ($\sin \theta_z \cos \phi$, $\sin \theta_z \sin \phi$, $\cos \theta_z$), where ϕ is the azimuthal angle with respect to the z axis. Following the scheme in ref 39, the equilibrium distribution of $\hat{n}$ is visualized by plotting (ϕ, $\cos(\theta_z)$), which reveals a nearly uniform distribution of molecular directions (Figure 2e). These indicate that molecules can rotate easily and sample a wide range of orientations at room temperature, consistent with previous studies.[23,37−42] We find that a significant amount of Pb atoms are displaced substantially (>0.1 Å) away from the center of I6 octahedra, while the distribution remains symmetric and is centered at zero displacement (Figure 2d). This is a signature of dynamical disorder.[60] Similarly, the orientations of local dipoles due to Pb displacement also exhibit nearly uniform distribution in the (ϕ, $\cos(\theta_z)$) map (Figure 2f).

Structural Response of MAPbI$_3$ to Electric and Stress Field. Structural changes due to an electric field applied along the +x direction are captured by the changes in $P(\mu_x)$, $P(\theta_x)$, and $P(\Delta_x^{Pb})$ (Figure 3). Molecular dipole alignment driven by electric field is observed: a higher electric field shifts the peak of $P(\mu_x)$ to higher values and the peak of $P(\theta_x)$ to lower values. The average value of Δ_x^{Pb} also becomes positive with increasing electric field. However, a relatively large electric field is required to introduce sizable ordering in MAPbI$_3$ at room temperature. For example, a large 1.0 MV/cm electric field, which is much larger than the coercive field of typical ferroelectric materials, such as BaTiO$_3$ or PbTiO$_3$, only increases the average value of Pb displacement, $\langle \Delta_x^{Pb} \rangle$, to 0.036 Å, and $P(\mu_x)$ and $P(\theta_x)$ still have broad distributions, suggesting the absence of perfect dipole alignment. This agrees with recent ab initio MD simulations in which no observable response of molecular dipoles within 20 ps for a field of magnitude 0.2 V/Å or lower is found.[61] Using a polarization value of 4.4×10^{-2} C/m^2 for MAPbI$_3$,[62] the energy gain ($2P_sE$, where P_s is the polarization) for 180° switching under 1 MV/cm electric field is ≈14 meV (a lattice constant of 6.29 Å is used), which is comparable to the energy scale of the molecular rotational barrier (MYP value, 36 meV; experimental value, 27 meV)[39,63] and thermal fluctuation (26 meV) at room temperature. Therefore, even under a relatively high electric field, molecules can still rotate to sample different configurations. The large configurational entropy thus suppresses the presence of long-range molecular ordering at room temperature.[43] This is in sharp contrast to polarization switching in ferroelectric PbTiO$_3$, where the polarization is an order of magnitude higher and the barrier height of the double well potential (>0.1 eV) is much larger, preventing thermal fluctuation-induced reverse switching. Describing MAPbI$_3$ as an Ising-like model assuming molecules can easily reorientate is likely to be oversimplified.[64] We further find that applying a 2% compressive epitaxial strain ($\eta = 0.02$) in the yz plane makes the molecules easier to align by electric field. A field of 1 MV/cm is enough to enhance substantially the probability for $P(\mu_x > 0)$ and $P(\theta_x < 90°)$ and to increase the value of $\langle \Delta_x^{Pb} \rangle$ to 0.067 Å, a 2-fold enhancement compared to the stress-free case.

Electrocaloric Effect in MAPbI$_3$. We estimated the adiabatic thermal changes upon the application of electric fields of different magnitudes along the x direction (Figure 4). The electric field is turned on gradually over a 10 ps period. With a high electric field (1 MV/cm), the induced change in temperature (ΔT) is relatively small (≈0.27 K), compared to $\Delta T = 12$ K observed for PbZr$_{0.95}$Ti$_{0.05}$O$_3$ thin films on application of electric fields of 0.48 MV/cm.[65] Increasing the magnitude of
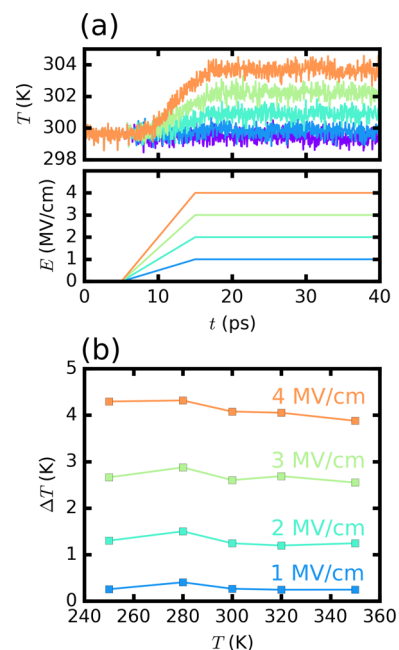
Figure 4. Electrocaloric effect in MAPbI$_3$. (a) Adiabatic thermal change in response to electric fields of different magnitudes. (b) Temperature and field dependence of the electrocaloric effect.

electric field to 4 MV/cm results in a larger ΔT of 4.1 K. Though higher fields up to 1.4 GV/m have been achieved in ultrathin crystal of barium titanate,[66] it is likely to be a challenge for MAPbI$_3$, which has a small band gap, to withstand ultrahigh electric fields. We further investigate the temperature dependence of ΔT from 250 to 350 K. As shown in Figure 4b, the ΔT remains almost constant for a given applied field. It is known that, for normal ferroelectrics, ΔT in general will peak around the phase transition temperature (T_c) and will shift toward a higher temperature as the electric field increases.[48] The weak temperature dependence of ΔT is usually found in relaxor ferroelectrics.[67] This hints at the structural similarity between MAPbI$_3$ and relaxor ferroelectrics with polar nanoscale domains.

To provide an atomistic description of the ECE in MAPbI$_3$, we analyze the distributions of molecular dipoles before and after adiabatically applying the field. The molecules initially have an isotropic distribution of orientations (Figure 5 inset, $E = 0$ MV/cm). By applying an electric field along the +x direction, the
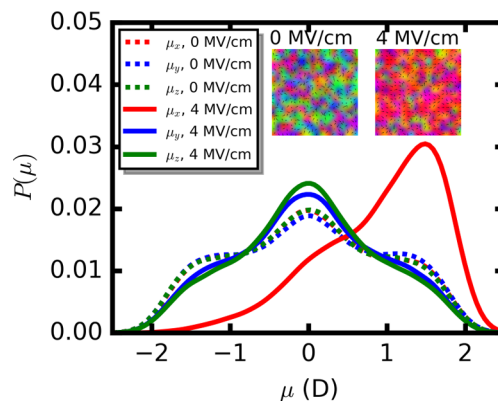
Figure 5. Probability distribution functions of molecular dipoles under E = 0 and 4 MV/cm. The inset shows the orientations of molecular dipoles obtained from molecular dynamics simulations at 300 K.

distribution of μ_x is heavily skewed in that direction. This corresponds to the formation of a more ordered structure, with dipoles aligning with the external electric field (Figure 5 inset, E = 4 MV/cm). Due to the conservation of total entropy in an adiabatic reversible process, the decrease of the configurational entropy (that characterizes the degree of order of atomic positions) is compensated by the increase of thermal entropy (that characterizes lattice vibrations), thus giving rise to the increase of temperature.

Strain Effect on Electrocaloric Effect. Previous studies have demonstrated that the epitaxial misfit strain can significantly affect the phase boundaries in ferroelectric thin films,[68−70] which could be used to tune the electrocaloric response.[71,72] We thus explore the effect of epitaxial strain on the ECE of MAPbI₃. In our MD simulations, a 2% and 4% compressive strain is applied in the yz plane, respectively, with the electric field applied along the x axis (the x-dimension of the supercell is allowed to relax). We find that the compressive epitaxial strain enhances the ECE by at least 2−3 times. For instance, $\Delta T(\eta=4\%)$ for E = 2 MV/cm at 300 K is about 5.2 K, which is about 4 times larger than that (1.3 K) in the free-standing case. Similarly, with a higher field (4 MV/cm), the temperature change can go up to 8.6 K under a 4% compressive epitaxial strain. Figure 6b shows the effect of
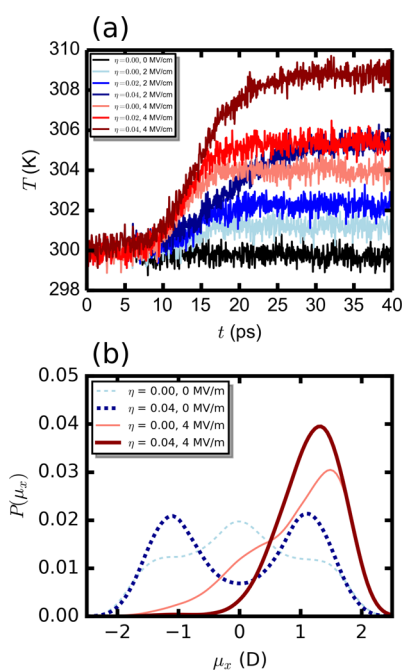
Figure 6. Influence of epitaxial strain on (a) electrocaloric effect and (b) probability distribution function of μ_x in MAPbI₃.

epitaxial strain on the probability distribution of μ_x. We find that, in the strained MAPbI₃ (η = 4%, E = 0 MV/cm), there are more molecular dipoles aligning along the x axis, as revealed by the enhanced peaks at both $\mu_x = −1.0$ and 1.0 D and the suppressed peak at μ_x = 0 D. Furthermore, compared to the freestanding MAPbI₃ under the same electric field, the epitaxially strained MAPbI₃ is closer to a single domain, as indicated by the nearly zero probability of $\mu_x < 0$ D. Therefore, the change of local polarization is significantly larger in strained MAPbI₃, which is responsible for the larger adiabatic thermal change.

Mechanocaloric Effect in MAPbI₃. The chemical bonds (Pb−I) in MAPbI₃ are not stiff,[53] because of the large lattice constants (5.7−6.3 vs 3.8−4.2 Å common for oxide perovskites)

and low oxidation state of halide anions (−1 vs −2 in oxide perovskites). The bulk modulus (10−25 GPa) is much smaller (at least tens of GPa) than values of typical oxide perovskites.[73,74] This suggests that MAPbI₃ is a "soft" solid and could be stretched/compressed with even a moderate stress. We examine the mechanocaloric response of MAPbI₃ to both uniaxial ($\Delta\sigma_u$) and isotropic stress ($\Delta\sigma_i$). In MD simulations, the uniaxial stress is applied by slowly increasing the cell dimension along the x axis while the dimensions along y and z directions are free to relax with stress maintained at 0 GPa. Figure 7a presents the
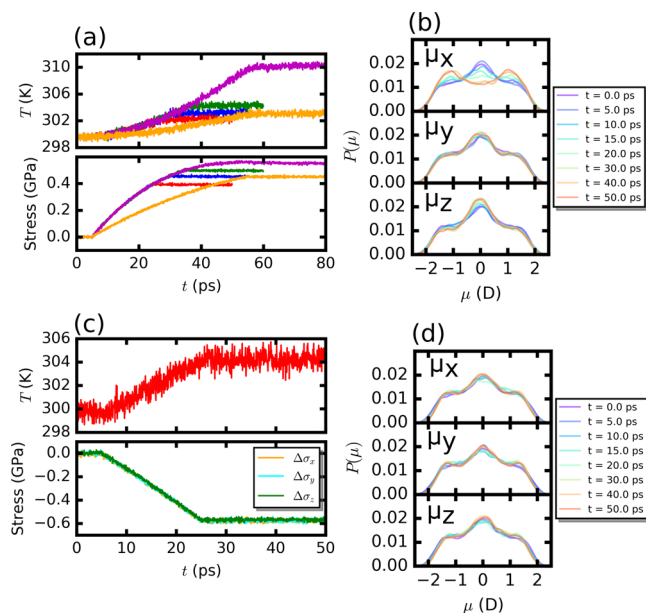
Figure 7. Mechanocaloric effect in MAPbI₃. (a) Adiabatic thermal change in response to uniaxial stress. (b) Time-resolved probability distribution functions of molecular dipoles for $\Delta\sigma_u$ = 0.45 GPa. (c) Adiabatic thermal change in response to an isotropic stress. (b) Time-resolved probability distribution functions of molecular dipoles for $\Delta\sigma_i$ = 0.57 GPa.

temperature profiles in response to the uniaxial stress of different loading speed and final magnitudes. It is found that stretching MAPbI₃ by the same amount with two different speeds (blue and orange lines in Figure 5a) results in similar changes in temperature (≈3.5 K for $\Delta\sigma_u$ = 0.45 GPa). Most notably, ΔT for $\Delta\sigma_u$ = 0.55 GPa is about 10.7 K, which is almost comparable to shape-memory alloys of Ni−Ti.[46,75] The evolution of the probability distribution functions of μ_x, μ_y, and μ_z under $\Delta\sigma_u$ = 0.45 GPa is shown in Figure 7b. We find that the rotation and alignment of molecular dipoles along the x axis, as characterized by the decreasing $P(\mu_x=0D)$ and increasing $P(\mu_x=\pm1.0D)$, is responsible for the temperature change. We also evaluate the values of ΔT for $\Delta\sigma_u$ = 0.45 GPa at temperatures 250, 280, 300, 320, and 350 K and find that the thermal changes vary from 3.3 to 3.8 K, showing weak temperature dependence. The heating caused by the isotropic compression is also significant (Figure 7c) in that the temperature increases by 4.5 K for $\Delta\sigma_i$ = 0.57 GPa, which corresponds to a 1% change in lattice constants. Under an isotropic stress, the probability distribution functions of molecular dipoles (Figure 7d) remain almost unchanged. This suggests that the increase in temperature is mainly due to the reduction of configuration entropy of a smaller volume.

Finally, we show the cooling steps upon the removal of various driving forces in Figure 8. Before removing the driving force, the
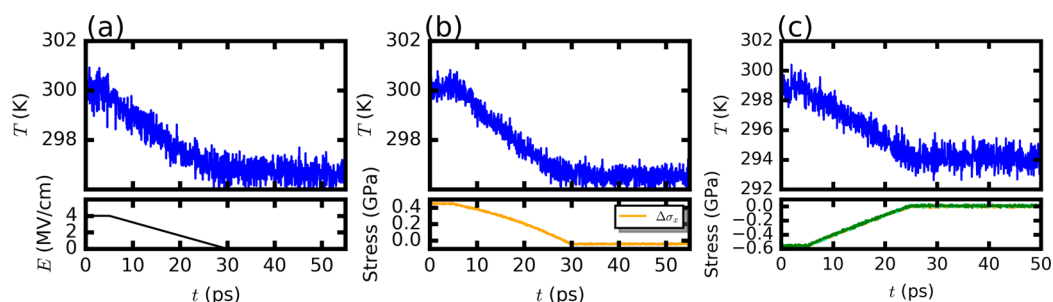
Figure 8. Simulated adiabatic cooling during the removal of (a) electric field, (b) uniaxial stress, and (c) isotropic stress.

supercell is first equilibrated to 300 K (heat ejection step). When the electric/stress field is gradually removed, the temperature goes down, eventually reaching a state with lower temperature, which could be used to load heat for cooling. Though previous studies show that MAPbI$_3$ has large dielectric loss,[76] which may lead to heating during charging/discharging, recent experiments demonstrate that crystallized MAPbI$_3$ can be optimized to a small dielectric loss of 0.02 at 1 MHz.[77]

CONCLUSION

In summary, our molecular dynamics simulations demonstrate that MAPbI$_3$ exhibits many typical caloric effects, which are due to the rearrangement of A-site molecular cations in response to electric and stress fields. The molecular dipoles have weak response to electric fields due to the small energy gain for dipole alignment and large configurational entropy at room temperature. Given the soft chemical bonds in MAPbI$_3$, we expect that the mechanocaloric effect is more likely to be observed experimentally. Organometal halide perovskites have demonstrated structural flexibility with varying atomic compositions and phase dimensionality.[78] The caloric response in these materials could be further enhanced through chemical doping. For example, replacing the CH$_3$NH$_3^+$ with a more polar cation is likely to increase the electrocaloric effect.

ASSOCIATED CONTENT

Ⓢ Supporting Information

The Supporting Information is available free of charge on the ACS Publications website at DOI: 10.1021/acs.jpcc.6b06416.

Pseudocubic lattice constant as a function of temperature (Figure S1) (PDF)

AUTHOR INFORMATION

Corresponding Authors

*S.L. e-mail: sliu@carnegiescience.edu.
*R.E.C. e-mail: rcohen@carnegiescience.edu.

Notes

The authors declare no competing financial interest.

ACKNOWLEDGMENTS

REFERENCES

(1) Kojima, A.; Teshima, K.; Shirai, Y.; Miyasaka, T. Organometal Halide Perovskites As Visible-Light Sensitizers for Photovoltaic Cells. *J. Am. Chem. Soc.* **2009**, 131, 6050−6051.

(2) Park, N.-G. Organometal Perovskite Light Absorbers Toward a 20% Efficiency Low-Cost Solid-State Mesoscopic Solar Cell. *J. Phys. Chem. Lett.* **2013**, 4, 2423−2429.

(3) Stranks, S. D.; Snaith, H. J. Metal-Halide Perovskites for Photovoltaic and Light-Emitting Devices. *Nat. Nanotechnol.* **2015**, 10, 391−402.

(4) NREL. Research Cell Efficiency Records. http://www.nrel.gov/ncpv/images/efficiency_chart.jpg.

(5) Saidaminov, M. I.; Abdelhady, A. L.; Murali, B.; Alarousu, E.; Burlakov, V. M.; Peng, W.; Dursun, I.; Wang, L.; He, Y.; Maculan, G.; Goriely, A.; Wu, T.; Mohammed, O. F.; Bakr, O. M. High-Quality Bulk Hybrid Perovskite Single Crystals within Minutes by Inverse Temperature Crystallization. *Nat. Commun.* **2015**, 6, 7586.

(6) Wang, Y.; Gould, T.; Dobson, J. F.; Zhang, H.; Yang, H.; Yao, X.; Zhao, H. Density Functional Theory Analysis of Structural and Electronic Properties of Orthorhombic Perovskite CH$_3$ NH$_3$ PbI$_3$. *Phys. Chem. Chem. Phys.* **2014**, 16, 1424−1429.

(7) Egger, D. A.; Kronik, L. Role of Dispersive Interactions in Determining Structural Properties of Organic−Inorganic Halide Perovskites: Insights from First-Principles Calculations. *J. Phys. Chem. Lett.* **2014**, 5, 2728−2733.

(8) He, Y.; Galli, G. Perovskites for Solar Thermoelectric Applications: A First Principle Study of CH$_3$NH$_3$AI$_3$ (*A* = Pb and Sn). *Chem. Mater.* **2014**, 26, 5394−5400.

(9) Mettan, X.; Pisoni, R.; Matus, P.; Pisoni, A.; Jaćimović, J.; Náfrádi, B.; Spina, M.; Pavuna, D.; Forró, L.; Horváth, E. Tuning of the Thermoelectric Figure of Merit of CH$_3$NH$_3$MI$_3$ (M = Pb, Sn) Photovoltaic Perovskites. *J. Phys. Chem. C* **2015**, 119, 11506−11510.

(10) Kim, M.; Im, J.; Freeman, A. J.; Ihm, J.; Jin, H. Switchable S = 1/2 and J = 1/2 Rashba Bands in Ferroelectric Halide Perovskites. *Proc. Natl. Acad. Sci. U. S. A.* **2014**, 111, 6900−6904.

(11) Zheng, F.; Tan, L. Z.; Liu, S.; Rappe, A. M. Rashba Spin−Orbit Coupling Enhanced Carrier Lifetime in CH$_3$NH$_3$PbI$_3$. *Nano Lett.* **2015**, 15, 7794−7800.

(12) Zhang, Q.; Ha, S. T.; Liu, X.; Sum, T. C.; Xiong, Q. Room-Temperature Near-Infrared High-Q Perovskite Whispering-Gallery Planar Nanolasers. *Nano Lett.* **2014**, 14, 5995−6001.

(13) Zhu, H.; Fu, Y.; Meng, F.; Wu, X.; Gong, Z.; Ding, Q.; Gustafsson, M. V.; Trinh, M. T.; Jin, S.; Zhu, X.-Y. Lead Halide Perovskite Nanowire Lasers With Low Lasing Thresholds and High Quality Factors. *Nat. Mater.* **2015**, 14, 636−642.

(14) Brivio, F.; Walker, A. B.; Walsh, A. Structural and Electronic Properties of Hybrid Perovskites for High-Efficiency Thin-Film Photovoltaics from First-Principles. *APL Mater.* **2013**, 1, 042111.

(15) Motta, C.; El-Mellouhi, F.; Kais, S.; Tabet, N.; Alharbi, F.; Sanvito, S. Revealing The Role of Organic Cations in Hybrid Halide Perovskite CH$_3$NH$_3$PbI$_3$. *Nat. Commun.* **2015**, 6, 7026.

(16) Frost, J. M.; Butler, K. T.; Brivio, F.; Hendon, C. H.; van Schilfgaarde, M.; Walsh, A. Atomistic Origins of High-Performance in Hybrid Halide Perovskite Solar Cells. *Nano Lett.* **2014**, 14, 2584−2590.

(17) Liu, S.; Zheng, F.; Koocher, N. Z.; Takenaka, H.; Wang, F.; Rappe, A. M. Ferroelectric Domain Wall Induced Band Gap Reduction and Charge Separation in Organometal Halide Perovskites. *J. Phys. Chem. Lett.* **2015**, *6*, 693−699.

(18) Ma, J.; Wang, L.-W. Nanoscale Charge Localization Induced by Random Orientations of Organic Molecules in Hybrid Perovskite CH$_3$NH$_3$PbI$_3$. *Nano Lett.* **2015**, *15*, 248−253.

(19) Etgar, L.; Gao, P.; Xue, Z.; Peng, Q.; Chandiran, A. K.; Liu, B.; Nazeeruddin, M. K.; Graetzel, M. Mesoscopic CH$_3$NH$_3$PbI$_3$/TiO$_2$ Heterojunction Solar Cells. *J. Am. Chem. Soc.* **2012**, *134*, 17396−17399.

(20) Lee, M. M.; Teuscher, J.; Miyasaka, T.; Murakami, T. N.; Snaith, H. J. Efficient Hybrid Solar Cells Based on Meso-Superstructured Organometal Halide Perovskites. *Science* **2012**, *338*, 643−647.

(21) Stoumpos, C. C.; Malliakas, C. D.; Kanatzidis, M. G. Semiconducting Tin and Lead Iodide Perovskites with Organic Cations: Phase Transitions, High Mobilities, and Near-Infrared Photoluminescent Properties. *Inorg. Chem.* **2013**, *52*, 9019−9038.

(22) Quarti, C.; Mosconi, E.; De Angelis, F. Structural and Electronic Properties of Organo-Halide Hybrid Perovskites from Ab Initio Molecular Dynamics. *Phys. Chem. Chem. Phys.* **2015**, *17*, 9394−9409.

(23) Chen, T.; Foley, B. J.; Ipek, B.; Tyagi, M.; Copley, J. R. D.; Brown, C. M.; Choi, J. J.; Lee, S.-H. Rotational Dynamics of Organic Cations in The CH$_3$NH$_3$PbI$_3$ Perovskite. *Phys. Chem. Chem. Phys.* **2015**, *17*, 31278−31286.

(24) Xiao, Z.; Yuan, Y.; Shao, Y.; Wang, Q.; Dong, Q.; Bi, C.; Sharma, P.; Gruverman, A.; Huang, J. Giant Switchable Photovoltaic Effect in Organometal Trihalide Perovskite Devices. *Nat. Mater.* **2015**, *14*, 193−198.

(25) Tress, W.; Marinova, N.; Moehl, T.; Zakeeruddin, S.; Nazeeruddin, M. K.; Grätzel, M. Understanding the Rate-Dependent *J − V* Hysteresis, Slow Time Component, and Aging in CH$_3$NH$_3$PbI$_3$ Perovskite Solar Cells: The Role of a Compensated Electric Field. *Energy Environ. Sci.* **2015**, *8*, 995−1004.

(26) Azpiroz, J. M.; Mosconi, E.; Bisquert, J.; De Angelis, F. Defect Migration in Methylammonium Lead Iodide and Its Role in Perovskite Solar Cell Operation. *Energy Environ. Sci.* **2015**, *8*, 2118−2127.

(27) Yang, D.; Ming, W.; Shi, H.; Zhang, L.; Du, M.-H. Fast Diffusion of Native Defects and Impurities in Perovskite Solar Cell Material CH$_3$NH$_3$PbI$_3$. *Chem. Mater.* **2016**, *28*, 4349−4357.

(28) Unger, E. L.; Hoke, E. T.; Bailie, C. D.; Nguyen, W. H.; Bowring, A. R.; Heumüller, T.; Christoforo, M. G.; McGehee, M. D. Hysteresis and Transient Behavior in Current−voltage Measurements of Hybrid-Perovskite Absorber Solar Cells. *Energy Environ. Sci.* **2014**, *7*, 3690−3698.

(29) Beilsten-Edmands, J.; Eperon, G. E.; Johnson, R. D.; Snaith, H. J.; Radaelli, P. G. Non-ferroelectric Nature of The Conductance Hysteresis in CH$_3$NH$_3$PbI$_3$ Perovskite-Based Photovoltaic Devices. *Appl. Phys. Lett.* **2015**, *106*, 173502.

(30) Meloni, S.; Moehl, T.; Tress, W.; Franckevičius, M.; Saliba, M.; Lee, Y. H.; Gao, P.; Nazeeruddin, M. K.; Zakeeruddin, S. M.; Rothlisberger, U.; Graetzel, M. Ionic Polarization-Induced Current−Voltage Hysteresis in CH$_3$NH$_3$PbX$_3$ Perovskite Solar Cells. *Nat. Commun.* **2016**, *7*, 10334.

(31) Kutes, Y.; Ye, L.; Zhou, Y.; Pang, S.; Huey, B. D.; Padture, N. P. Direct Observation of Ferroelectric Domains in Solution-Processed CH$_3$NH$_3$PbI$_3$ Perovskite Thin Films. *J. Phys. Chem. Lett.* **2014**, *5*, 3335−3339.

(32) Kim, H.-S.; Kim, S. K.; Kim, B. J.; Shin, K.-S.; Gupta, M. K.; Jung, H. S.; Kim, S.-W.; Park, N.-G. Ferroelectric Polarization in CH$_3$NH$_3$PbI$_3$ Perovskite. *J. Phys. Chem. Lett.* **2015**, *6*, 1729−1735.

(33) Chen, B.; Shi, J.; Zheng, X.; Zhou, Y.; Zhu, K.; Priya, S. Ferroelectric Solar Cells Based on Inorganic−Organic Hybrid Perovskites. *J. Mater. Chem. A* **2015**, *3*, 7699−7705.

(34) Fan, Z.; Xiao, J.; Sun, K.; Chen, L.; Hu, Y.; Ouyang, J.; Ong, K. P.; Zeng, K.; Wang, J. Ferroelectricity of CH$_3$NH$_3$PbI$_3$ Perovskite. *J. Phys. Chem. Lett.* **2015**, *6*, 1155−1161.

(35) Coll, M.; Gomez, A.; Mas-Marza, E.; Almora, O.; Garcia-Belmonte, G.; Campoy-Quiles, M.; Bisquert, J. Polarization Switching

and Light-Enhanced Piezoelectricity in Lead Halide Perovskites. *J. Phys. Chem. Lett.* **2015**, *6*, 1408−1413.

(36) Weller, M. T.; Weber, O. J.; Henry, P. F.; Di Pumpo, A. M.; Hansen, T. C. Complete Structure and Cation Orientation in the Perovskite Photovoltaic Methylammonium Lead Iodide Between 100 and 352 K. *Chem. Commun.* **2015**, *51*, 4180−4183.

(37) Mosconi, E.; Quarti, C.; Ivanovska, T.; Ruani, G.; De Angelis, F. Structural and Electronic Properties of Organo-Halide Lead Perovskites: A Combined IR-Spectroscopy and Ab Initio Molecular Dynamics Investigation. *Phys. Chem. Chem. Phys.* **2014**, *16*, 16137−16144.

(38) Carignano, M. A.; Kachmar, A.; Hutter, J. Thermal Effects on CH$_3$NH$_3$PbI$_3$ Perovskite from Ab Initio Molecular Dynamics Simulations. *J. Phys. Chem. C* **2015**, *119*, 8991−8997.

(39) Mattoni, A.; Filippetti, A.; Saba, M. I.; Delugas, P. Methylammonium Rotational Dynamics in Lead Halide Perovskite by Classical Molecular Dynamics: The Role of Temperature. *J. Phys. Chem. C* **2015**, *119*, 17421−17428.

(40) Wasylishen, R.; Knop, O.; Macdonald, J. Cation Rotation in Methylammonium Lead Halides. *Solid State Commun.* **1985**, *56*, 581−582.

(41) Poglitsch, A.; Weber, D. Dynamic Disorder in Methylammoniumtrihalogenoplumbates (II) Observed by Millimeter-Wave Spectroscopy. *J. Chem. Phys.* **1987**, *87*, 6373−6378.

(42) Leguy, A. M. A.; Frost, J. M.; McMahon, A. P.; Sakai, V. G.; Kochelmann, W.; Law, C.; Li, X.; Foglia, F.; Walsh, A.; O'Regan, B. C.; Nelson, J.; Cabral, J. T.; Barnes, P. R. F. The Dynamics of Methylammonium Ions in Hybrid Organic−Inorganic Perovskite Solar Cells. *Nat. Commun.* **2015**, *6*, 7124.

(43) Filippetti, A.; Delugas, P.; Saba, M. I.; Mattoni, A. Entropy-Suppressed Ferroelectricity in Hybrid Lead-Iodide Perovskites. *J. Phys. Chem. Lett.* **2015**, *6*, 4909−4915.

(44) Scott, J. F. Electrocaloric Materials. *Annu. Rev. Mater. Res.* **2011**, *41*, 229−240.

(45) Takeuchi, I.; Sandeman, K. Solid-State Cooling with Caloric Materials. *Phys. Today* **2015**, *68*, 48−53.

(46) Moya, X.; Kar-Narayan, S.; Mathur, N. D. Caloric Materials Near Ferroic Phase Transitions. *Nat. Mater.* **2014**, *13*, 439−450.

(47) Valant, M. Electrocaloric Materials for Future Solid-State Refrigeration Technologies. *Prog. Mater. Sci.* **2012**, *57*, 980−1009.

(48) Rose, M. C.; Cohen, R. E. Giant Electrocaloric Effect Around T_c. *Phys. Rev. Lett.* **2012**, *109*, 187604.

(49) Pirc, R.; Kutnjak, Z.; Blinc, R.; Zhang, Q. M. Electrocaloric Effect in Relaxor Ferroelectrics. *J. Appl. Phys.* **2011**, *110*, 074113.

(50) Lu, S. G.; Rožič, B.; Zhang, Q. M.; Kutnjak, Z.; Li, X.; Furman, E.; Gorny, L. J.; Lin, M.; Malič, B.; Kosec, M.; Blinc, R.; Pirc, R. Organic and Inorganic Relaxor Ferroelectrics with Giant Electrocaloric Effect. *Appl. Phys. Lett.* **2010**, *97*, 162904.

(51) Kutnjak, Z.; Petzelt, J.; Blinc, R. The Giant Electromechanical Response in Ferroelectric Relaxors as a Critical Phenomenon. *Nature* **2006**, *441*, 956−959.

(52) Mattoni, A.; Filippetti, A.; Saba, M.; Caddeo, C.; Delugas, P. Temperature Evolution of Methylammonium Trihalide Vibrations at the Atomic Scale. *J. Phys. Chem. Lett.* **2016**, *7*, 529−535.

(53) Egger, D. A.; Rappe, A. M.; Kronik, L. Hybrid Organic−Inorganic Perovskites on the Move. *Acc. Chem. Res.* **2016**, *49*, 573−581.

(54) Chang, Y.; Park, C.; Matsuishi, K. First-Principles Study of the Structural and the Electronic Properties of the Lead-Halide-Based Inorganic−Organic Perovskites (CH$_3$NH$_3$)PbX$_3$ and CsPbX$_3$ (X = Cl, Br, I). *J. Korean Phys. Soc.* **2004**, *44*, 889−893.

(55) Du, M. H. Efficient Carrier Transport in Halide Perovskites: Theoretical Perspectives. *J. Mater. Chem. A* **2014**, *2*, 9091−9098.

(56) Plimpton, S. Fast Parallel Algorithms for Short-Range Molecular Synamics. *J. Comput. Phys.* **1995**, *117*, 1−19.

(57) Todorov, I. T.; Smith, W.; Trachenko, K.; Dove, M. T. DL_POLY_3: new dimensions in molecular dynamics simulations via massive parallelism. *J. Mater. Chem.* **2006**, *16*, 1911.

(58) Hockney, R.; Eastwood, J. *Computer Simulation Using Particles*; CRC Press: Boca Raton, FL, 1989.

(59) Baikie, T.; Fang, Y.; Kadro, J. M.; Schreyer, M.; Wei, F.; Mhaisalkar, S. G.; Graetzel, M.; White, T. J. Synthesis and Crystal Chemistry of the Hybrid Perovskite $(CH_3NH_3)PbI_3$ for Solid-State Sensitised Solar Cell Applications. *J. Mater. Chem. A* **2013**, *1*, 5628−5641.

(60) Yaffe, O.; Guo, Y.; Hull, T.; Stoumpos, C. C.; Tan, L. Z.; Egger, D. A.; Zheng, F.; Semonin, O. E.; Beecher, A. N.; Heinz, T. F.; Kronik, L. The Nature of Dynamic Disorder in Lead Halide Perovskite Crystals. *arXiv.org, e-Print Arch., Condens. Matter* **2016**, arXiv:1604.08107.

(61) Goehry, C.; Nemnes, G. A.; Manolescu, A. Collective Behavior of Molecular Dipoles in CH 3 NH 3 PbI 3. *J. Phys. Chem. C* **2015**, *119*, 19674−19680.

(62) Stroppa, A.; Quarti, C.; De Angelis, F.; Picozzi, S. Ferroelectric Polarization of CH 3 NH 3 PbI 3: A Detailed Study Based on Density Functional Theory and Symmetry Mode Analysis. *J. Phys. Chem. Lett.* **2015**, *6*, 2223−2231.

(63) Onoda-Yamamuro, N.; Yamamuro, O.; Matsuo, T.; Suga, H. p-T Phase Relations of $CH_3NH_3PbX_3$ (X = Cl, Br, I) Crystals. *J. Phys. Chem. Solids* **1992**, *53*, 277−281.

(64) Frost, J. M.; Butler, K. T.; Walsh, A. Molecular Ferroelectric Contributions to Anomalous Hysteresis in Hybrid Perovskite Solar Cells. *APL Mater.* **2014**, *2*, 081506.

(65) Mischenko, A. S.; Zhang, Q.; Scott, J. F.; Whatmore, R. W.; Mathur, N. D. Giant Electrocaloric Effect in Thin-Film $PbZr_{0.95}Ti_{0.05}O_3$. *Science* **2006**, *311*, 1270−1271.

(66) Morrison, F. D.; Zubko, P.; Jung, D. J.; Scott, J. F.; Baxter, P.; Saad, M. M.; Bowman, R. M.; Gregg, J. M. High-Field Conduction in Barium Titanate. *Appl. Phys. Lett.* **2005**, *86*, 152903.

(67) Goupil, F. L.; Axelsson, A.-K.; Dunne, L. J.; Valant, M.; Manos, G.; Lukasiewicz, T.; Dec, J.; Berenov, A.; Alford, N. M. Anisotropy of the Electrocaloric Effect in Lead-Free Relaxor Ferroelectrics. *Adv. Energy Mater.* **2014**, *4*, 1301688.

(68) Pertsev, N. A.; Zembilgotov, A. G.; Tagantsev, A. K. Effect of Mechanical Boundary Conditions on Phase Diagrams of Epitaxial Ferroelectric Thin Films. *Phys. Rev. Lett.* **1998**, *80*, 1988−1991.

(69) Choi, K. J. Enhancement of Ferroelectricity in Strained $BaTiO_3$ Thin Films. *Science* **2004**, *306*, 1005−1009.

(70) Alpay, S. P. Structural Characteristics of Ferroelectric Phase Transformations in Single-Domain Epitaxial Films. *J. Appl. Phys.* **2004**, *95*, 8118.

(71) Akcay, G.; Alpay, S. P.; Rossetti, G. A., Jr; Scott, J. Influence of Mechanical Boundary Conditions on The Electrocaloric Properties of Ferroelectric Thin Films. *J. Appl. Phys.* **2008**, *103*, 024104.

(72) Liu, Y.; Wei, J.; Lou, X.; Bellaiche, L.; Scott, J. F.; Dkhil, B. Influence of Epitaxial Strain on Elastocaloric Effect in Ferroelectric Thin Films. *Appl. Phys. Lett.* **2015**, *106*, 032901.

(73) Feng, J. Mechanical Properties of Hybrid Organic-Inorganic $CH_3NH_3BX_3$ (B = Sn, Pb; X = Br, I) Perovskites for Solar Cell Absorbers. *APL Mater.* **2014**, *2*, 081801.

(74) Sun, S.; Fang, Y.; Kieslich, G.; White, T. J.; Cheetham, A. K. Mechanical Properties of Organic−Inorganic Halide Perovskites, $CH_3NH_3PbX_3$ (X = I, Br and Cl), by Nanoindentation. *J. Mater. Chem. A* **2015**, *3*, 18450−18455.

(75) Cui, J.; Wu, Y.; Muehlbauer, J.; Hwang, Y.; Radermacher, R.; Fackler, S.; Wuttig, M.; Takeuchi, I. Demonstration of High Efficiency Elastocaloric Cooling with Large ΔT using NiTi Wires. *Appl. Phys. Lett.* **2012**, *101*, 073904.

(76) Lin, Q.; Armin, A.; Nagiri, R. C. R.; Burn, P. L.; Meredith, P. Electro-optics of Perovskite Solar Cells. *Nat. Photonics* **2014**, *9*, 106−112.

(77) Kim, Y.-J.; Dang, T.-V.; Choi, H.-J.; Park, B.-J.; Eom, J.-H.; Song, H.-A.; Seol, D.; Kim, Y.; Shin, S.-H.; Nah, J.; Yoon, S.-G. Piezoelectric Properties of $CH_3NH_3PbI_3$ Perovskite Thin Films and Their Applications in Piezoelectric Generators. *J. Mater. Chem. A* **2016**, *4*, 756−763.

(78) Zheng, F.; Saldana-Greco, D.; Liu, S.; Rappe, A. M. Material Innovation in Advancing Organometal Halide Perovskite Functionality. *J. Phys. Chem. Lett.* **2015**, *6*, 4862−4872.

(79) Delugas, P.; Caddeo, C.; Filippetti, A.; Mattoni, A. Thermally Activated Point-Defects Diffusion in Methylammonium Lead Trihalide: Anisotropic and Ultra-High Mobility of Iodine. *J. Phys. Chem. Lett.* **2016**, *7*, 2356−2361.